

# Synthesis of antibacterial composite coating containing nanocapsules in an atmospheric pressure plasma

Lei Wang<sup>a,\*</sup>, Chiara Lo Porto<sup>b</sup>, Fabio Palumbo<sup>c,\*</sup>, Martina Modic<sup>d</sup>, Uroš Cvelbar<sup>d</sup>, Rouba Ghobeira<sup>a</sup>, Nathalie De Geyter<sup>a</sup>, Mike De Vrieze<sup>e</sup>, Špela Kos<sup>f</sup>, Gregor Serša<sup>f</sup>, Christophe Leys<sup>a</sup>, Anton Nikiforov<sup>a</sup>

<sup>a</sup> Department of Applied Physics, Ghent University, Sint-Pietersnieuwstraat 41 B4, 9000 Ghent, Belgium

<sup>b</sup> Department of Chemistry, University of Bari "Aldo Moro", Via Orabona 4, 70126 Bari, Italy

<sup>c</sup> Institute of Nanotechnology, National Research Council of Italy, Department of Chemistry, University of Bari "Aldo Moro", Via Orabona 4, 70126 Bari, Italy

<sup>d</sup> Laboratory for Gaseous Electronics, Jozef Stefan Institute, Jamova cesta 39, 1000 Ljubljana, Slovenia

<sup>e</sup> Centexbel, Technologiepark 70, 9052 Zwijnaarde, Belgium

<sup>f</sup> Department of Experimental Oncology, Institute of Oncology Ljubljana, Zaloška cesta 2, 1000 Ljubljana, Slovenia

## ARTICLE INFO

### Keywords:

Aerosol-assisted deposition  
Atmospheric pressure plasma  
Nanocapsule  
Antibacterial coating  
Nanocomposite

## ABSTRACT

Antibacterial coating is an important strategy preventing bacterial colonization and biofilm formation. One-step synthesis of nanocapsule-containing antibacterial coatings with controlled release of Ag<sup>+</sup> ions was achieved in the current work by aerosol-assisted atmospheric pressure plasma deposition. The experimental parameters of deposition including the discharge power, silver nitrate concentration, aerosol flow rate, continuous and pulsed mode of operation were studied in order to analyze their effects on surface morphology and chemical composition of the coating. Formation of nanocapsules embedded in the polymeric coating was observed. A core-shell structure was found for nanocapsule with silver in the core and polymer in the shell. Antibacterial coatings on polyethylene terephthalate film were studied in terms of Ag<sup>+</sup> ion release, antibacterial properties against *Escherichia coli* and *Staphylococcus aureus*, and cytotoxicity with murine fibroblasts. Two-phase release kinetics of Ag<sup>+</sup> ions was observed as initially a short-term burst release followed by a long-term slow release. It was revealed that high antibacterial efficiency of the coatings deposited on polyethylene terephthalate films can be coupled with low cytotoxicity. These biocompatible antibacterial coatings are very promising in different fields including biological applications.

## 1. Introduction

Nowadays antibacterial coatings are rapidly emerging as the main mitigation strategy against pathogenic bacteria [1,2]. The nosocomial infections from the hospital and the original condition of patients bring global challenges to the hospitals and healthcare services [1,3]. Nosocomial infections are primarily induced from bacterial colonization of biomedical surfaces, to form a biofilm as a reservoir of pathogens. Although antibiotics have been utilized worldwide, increasing antibiotic resistance presents a global threat to public health [4]. Antibacterial coatings arise as an important approach to restrict the nosocomial infection rate without side effects and the development of antibiotic resistance. Ag-containing coatings are by far the most prevailing antibacterial nanomaterials [1,5], due to the advantages of broad antibacterial spectrum efficacy, low systemic absorption of Ag<sup>+</sup> ions

with tissue cells, satisfactory stability [1]. However, Ag-containing coatings and released Ag<sup>+</sup> may also affect the tissue cells, which requires the control and regulation of dosage to avoid cytotoxicity side effects. Therefore, release-controllable biocompatible antibacterial coatings are desired for medical applications. A combination of initial burst-release and followed slow release can be advantageous for many medical applications since the burst release is beneficial for the antibacterial protection in the early stage and long-term slow release is needed to prolong the lifetime of antibacterial coatings. However, simple embedding Ag into layer structured coating is often unable to achieve such combined two-phase release kinetics.

Traditional "wet" chemistry methods are used for producing Ag-containing coatings while exhibiting the drawbacks including tedious multi-step synthesis, hazardous solvents and reactants, and high process costs [6]. Plasma-based methods are attractive to produce Ag-

\* Corresponding authors.

E-mail addresses: [wanglei09c@163.com](mailto:wanglei09c@163.com) (L. Wang), [fabio.palumbo@cnr.it](mailto:fabio.palumbo@cnr.it) (F. Palumbo).

<https://doi.org/10.1016/j.msec.2020.111496>

Received 28 January 2020; Received in revised form 31 August 2020; Accepted 6 September 2020

Available online 09 September 2020

0928-4931/ © 2020 Elsevier B.V. All rights reserved.

containing coatings, due to the advantages including relatively simple engineering, extraordinary versatility, solvent-free deposition, and the possibility of large scale production [7]. Aerosol-assisted atmospheric pressure plasma deposition (AAPPD) stands out to be a novel method to produce nano-/biocomposite coatings with core-shell structured nanocapsules [8–10]. Recently, Lo Porto et al. succeeded in the synthesis of vancomycin-containing nanocapsules for drug delivery applications using AAPPD [11,12]. Palumbo et al. synthesized lysozyme-embedded bio-composite thin films and gentamicin-containing nanocapsules through AAPPD [8,13]. With the possibility to produce core-shell structured nanocapsules, AAPPD brings a new perspective to deposit Ag-containing antibacterial coatings. To the best of our knowledge, this approach for engineering Ag-containing coatings has not been reported yet.

In this work, AAPPD was applied to produce release-controllable Ag-containing antibacterial coatings in a single-step synthesis. It has to be emphasized that Ag-containing nanocomposite was directly produced during the deposition step from the pristine  $\text{AgNO}_3$  solution, which brings unique advantages to this method compared with other techniques. The whole deposition is a one-step sustainable process with very limited use of nontoxic chemicals as it does not require preformed expensive and toxic nanoparticle dispersions, which has a potential of large scale environmentally friendly production with very limited use of chemicals. First, Ag-containing coatings were deposited on silicon wafers and investigated in terms of surface morphology and chemistry. Based on the analyses of the coating, a hypothesis of the deposition mechanism of AAPPD was proposed. Since PET films are used as materials in many medical applications, the working conditions were optimized for PET films and tuned to control the  $\text{Ag}^+$  ion release by changing the aerosol gas flow ratio. Finally, the release rate of  $\text{Ag}^+$  ions, antibacterial tests with Gram-negative bacteria (*Escherichia coli*) and Gram-positive bacteria (*Staphylococcus aureus*), cytotoxicity assay with murine fibroblasts were carried out to explore biological applications of the novel biocompatible antibacterial coatings.

## 2. Experimental methods

### 2.1. Materials

Helium 99.999% (Air Liquide) was used as the carrier gas in the plasma processes. Liquid hexamethyldisiloxane (HMDSO, Sigma-Aldrich) and silver nitrate ( $\text{AgNO}_3$ , Sigma-Aldrich) solution in water of Milli-Q quality (Millipore, Bedford, MA) were applied to produce aerosols. During the deposition, two kinds of substrate were used: shards ( $1 \times 1 \text{ cm}^2$ ) of  $710 \mu\text{m}$  thick double-side polished silicon wafers (MicroChemicals GmbH) and non-woven polyethylene terephthalate (PET) films (DuPont,  $1.5 \times 6 \text{ cm}^2$ ) with a thickness of 0.2 mm. Polycarbonate (PC, Goodfellow,  $1 \times 1 \text{ cm}^2$ ) films with a thickness of 0.25 mm were used as substrates in the deposition for energy dispersive X-ray spectroscopy.

### 2.2. Aerosol-assisted atmospheric pressure plasma treatment

The aerosol-assisted atmospheric pressure plasma treatment system consists of a dielectric barrier discharge (DBD) plasma source, aerosol generation system, gas flow control unit, and power generator. This DBD plasma source has been reported elsewhere [11–13]. As shown in Fig. 1, it had two planar metal electrodes ( $5 \times 8 \text{ cm}^2$ ), both covered by 0.63 mm thick alumina sheets. The gap between the two sheets was set at 3 mm. The DBD plasma source was placed in a sealed Plexiglas chamber to confine the gas flow and avoid ambient air impurities. The gas flow rate was controlled with a mass flow controller (MSK instruments). HMDSO (Monomer), and  $\text{AgNO}_3$  solution were injected into the plasma reactor through two separated pneumatic atomizers (model 3076, TSI) fed with helium gas flow.  $\text{AgNO}_3$  aqueous solution was diluted to concentration of 10 mmol/L (low concentration, LC) or

100 mmol/L (high concentration, HC). The aerosol droplets had diameters in the range of sub-micrometers, which was reported by others at similar conditions [8,11].

The feeding gas/aerosol flew from an inlet on one side of the DBD plasma source, through the plasma zone and was afterward pumped out by an aspirator on the opposite side of the reactor. The discharge was sustained in continuous mode (CM) and pulsed mode (PM) by using a power supply at 24 kHz (PVM500, Information Unlimited) and pulse generator. The pulsed mode corresponded to a duty cycle of 33%, with ON time of 40 ms and OFF time of 80 ms. The discharge current and voltage waveforms were acquired by an oscilloscope (TDS 2014C, Tektronix) connected with a resistance-type current probe and a high-voltage (P6015A, Tektronix) probe. Experiments were performed at two power levels: high power density (HP) of  $0.76 \text{ W/cm}^2$  and low power density (LP) of  $0.38 \text{ W/cm}^2$ . The substrates were placed on the bottom electrode, at a distance of 3 cm from the inlet. Before each deposition, a purging process of the chamber was performed with pure helium with a flow rate of 4 SLM for 3 min. After deposition of 10 min, the samples were taken out for further analysis.

The AAPPD treatment was applied in experiments in the following way as presented in Fig. 2. First, the deposition was done on silicon wafers at various experimental conditions to study surface morphology and chemistry as shown in Table 1. After the optimization of the experimental parameters, the deposition was performed on PET films to investigate antibacterial activity for biomedical applications. The treatment process was further optimized to achieve the desired performance, as shown in Table 2.

### 2.3. Surface characterization

Surface profilometry was carried out to obtain the coating thickness by an  $\alpha$ -step profilometer D120 (Tencor-Instruments). Surface wettability was evaluated by static water contact angle (WCA) measuring with  $5 \mu\text{L}$  double-distilled water droplets (ramé-hart Inc., 100 goniometer).

Fourier transform infrared spectroscopy (FTIR) was conducted to characterize the functional groups of the coatings. FTIR spectra were obtained with a Vertex 70 V Bruker spectrometer at  $4 \text{ cm}^{-1}$  resolution and 32 scans per analysis. Before each acquisition, the spectrometer was evacuated to  $< 150 \text{ Pa}$  for 10 min.

Scanning electron microscopy (SEM) was implemented to investigate the surface morphology of the coatings with a Zeiss Supra 40 SEM with a Gemini field-effect emission gun. SEM was carried out at an accelerating voltage of 3 kV and samples were sputter-coated with a 20 nm thick Cr layer. Energy dispersive X-ray spectroscopy (EDX) detector was integrated with SEM and used to check the spatial distribution of elements in the coating.

X-ray photoelectron spectroscopy (XPS) was performed to study chemical composition with a PHI-5600 VersaProbe-spectrometer, using a monochromatic  $\text{Al K}_{\alpha}$  X-ray source operating at 150 W. Survey scans were recorded at 115 eV pass energy. Charge compensation of the samples was performed with a flood gun (18 mA emission current; 40 eV electron energy). The hydrocarbon component of the C1s spectrum was set at  $284.8 \pm 0.2 \text{ eV}$  to calibrate the binding energy scale. XPS spectra were analyzed with MultiPack software.

### 2.4. Ion release tests

Inductively coupled plasma mass spectroscopy (ICP-MS) was employed to investigate the cumulative release of  $\text{Ag}^+$  ions. Agilent Technologies 7700 Series was used with a liquid sample introduction by a PFA micro-nebulizer. Indium and rhenium for internal standardization were chosen to calibrate the aqueous multi-element solutions. Each sample was cut into an area of  $9 \text{ cm}^2$  and weighted, then immersed in air-saturated 200 mL deionized water in an Erlenmeyer flask. Afterward, the Erlenmeyer flask was shaken at 100 rpm. The  $\text{Ag}^+$  ion

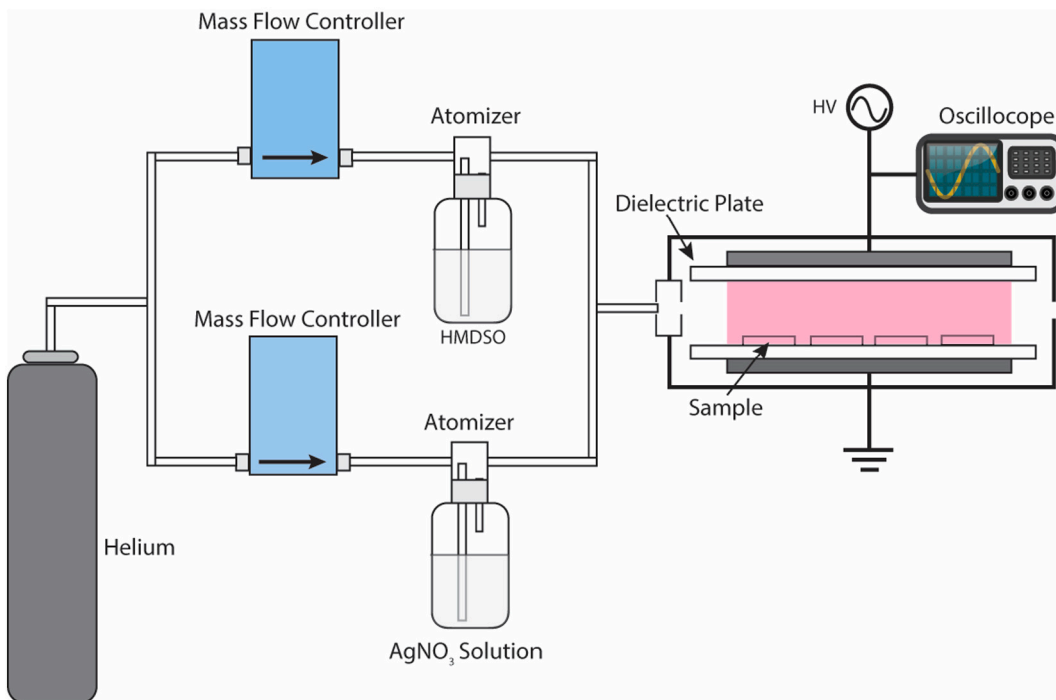


Fig. 1. Scheme of the experimental setup for aerosol-assisted atmospheric pressure deposition.

release rate was measured by taking out 15 mL solution from the flask to a vial at room temperature. Isotope <sup>107</sup>Ag was used as a recommended mass for the octopole detection system.

2.5. Antibacterial tests

Antibacterial testing was performed with a modified ISO 20743-2005 standard to determine the antibacterial activity of PET films. PET films were cut in squares of 1 × 1 cm<sup>2</sup> size. 3 samples, including control, were placed in 24-well cell culture plates. Samples were inoculated with 50 μL of bacterial solution with the 10<sup>5</sup> CFU/mL. Tests were performed with two different bacterial strains: *Escherichia coli* ATCC25922 and *Staphylococcus aureus* ATCC25923. After the incubation period of 24 h, samples were aseptically transferred to a Falcon tube containing 5 mL of sterile TSB medium and bacteria were removed from the samples using VibraMix shaker at 2000 rpm. This suspension was used to prepare 10-fold serial dilutions, which were plated out for the determination of viable counts. After incubation for 24 h at 37 °C, the number of colony-forming units was counted. The antibacterial activity of PET films was calculated compared to the control samples, where no coating was deposited. A macrodilution method was adopted to test the antibacterial performances. The reduction of bacteria R was defined as R = (B - A) / B to indicate the biostatic efficacy originating from the contact with treated samples, where A, B are treated sample and control sample after incubation, respectively.

The XTT assay (Merck KGaA, Darmstadt, Germany) was conducted according to the protocol described in the reference [14, 15]. 50 μL

Table 1

Deposition conditions for engineering samples on silicon wafers. Samples F and G are both used as controls with no AgNO<sub>3</sub> addition. AgNO<sub>3</sub> solution of 100 mmol/L was used in this work except when explicitly indicated (sample D). 100% and 33% duty cycle correspond to the continuous mode and pulsed mode, respectively.

Sample	Aerosol flow rate/SLM		Power (W/cm <sup>2</sup> )	Duty cycle
	HMDSO	AgNO <sub>3</sub>		
A	3	3	0.76	100%
B	1	5	0.76	100%
C	1	5	0.38	100%
D	1	5 (10 mmol/L)	0.76	100%
E	1	5	0.76	33%
F	1	5 (100% H <sub>2</sub> O)	0.76	33%
G	1	5 (No aerosol)	0.76	33%

samples of each bacterial solution that was prepared as described above were transferred to the wells of a 96-well plate containing 20 μL of XTT stock solution and 50 μL of TSB solution. The metabolic activity of bacteria was measured using a microplate reader (Spark 10 M, Tecan, Männedorf, CH) and was presented as absorbance at 450 nm.

2.6. Cytotoxicity assay

Murine fibroblasts L929 (American Type Culture Collection, USA) were cultured in advanced minimum essential medium (AMEM, Life

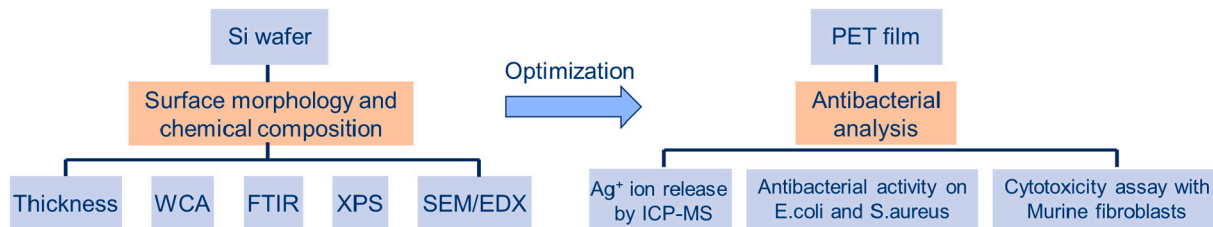


Fig. 2. Diagram for deposition on flat substrates from Si wafers to PET films.

**Table 2**

Aerosol flow rates used for deposition on PET film samples. The samples are treated for 10 min with a duty cycle of 33% at HP mode. The samples are labeled according to the samples on Si wafer (e.g. deposition condition of sample F-FL4 is identical to sample F in Table 4 except the substrate).

Sample	Flow rate/SLM	
	HMDSO	AgNO <sub>3</sub>
E-FL1	1	5
E-FL2	2	4
E-FL3	3	3
F-FL4	1	5 (100% H <sub>2</sub> O)
G-FL5	1	5 (No aerosol)

Technologies, USA) supplemented with 10 mM/L L-glutamine, 5% FBS, 50 mg/mL gentamicin, and 100 U/mL penicillin. The cells were cultured at 37 °C in a 5% CO<sub>2</sub> humidified incubator and were maintained in monolayers until they reached 80–90% confluence.

Cytotoxicity test was performed according to ISO 10993-5 standard (biological evaluation of medical devices; tests for in vitro cytotoxicity). Samples with an area of 3 cm<sup>2</sup> were incubated in cell medium for 24 h. Uncoated PET films were used as controls. Extracts were used for incubation with cells for an additional 24, 48, and 72 h. The cytotoxicity of PET film samples was quantified using PrestoBlue Cell Viability Reagent. Cells were incubated in a 5% CO<sub>2</sub> humidified incubator at 37 °C for 24 h. After incubation, the media was removed and replaced with PrestoBlue Viability Reagent (Life Technologies, USA), and diluted in cell media. After further incubation for 30 min, the fluorescent intensity was recorded with a microplate reader (Infinite 200, Tecan, CH). The survival of cells was normalized to the control group of cells, that were incubated with the non-exposed medium.

Cells for microscopy images were incubated with medium extracts for 24 h at 37 °C as described above. After incubation, the media was replaced and cells were stained using LIVE/DEAD Cell Viability Kit (ThermoFisher Scientific, Waltham, MA, USA) according to the manufacturer's protocol. Images were captured with a fluorescent microscope (IX-70 Olympus, Germany) under 10× magnification.

## 2.7. Statistical analysis

Statistical analyses of the results were performed with GraphPad Prism 8.1.2 software (GraphPad Software Inc., USA). Statistical significance was evaluated using a one-way analysis of variance (ANOVA) test. Dunnett post-test was performed comparing control samples versus all other samples for both bacteria separately. For cytotoxic effects, the viability of cells was normalized according to the control group (Ctrl), where cells were incubated under the standard protocol, with original medium, not exposed to any film material. Statistical analysis was performed as described above. A *p*-value of < 0.05 was considered statistically significant.

## 3. Results and discussion

In the first step, Si wafer was used as a flat substrate to deposit coatings and investigate the surface morphology and chemical composition under different working conditions. Then the optimized deposition conditions were applied for engineering coatings on PET films. The Ag<sup>+</sup> ion release, antibacterial tests, and cytotoxicity assay were further performed to get an insight into properties and functionality of novel antibacterial coatings for medical applications.

### 3.1. Surface morphology and chemistry

#### 3.1.1. Coatings thickness and water contact angle

Coatings thickness is an important factor in the deposition process

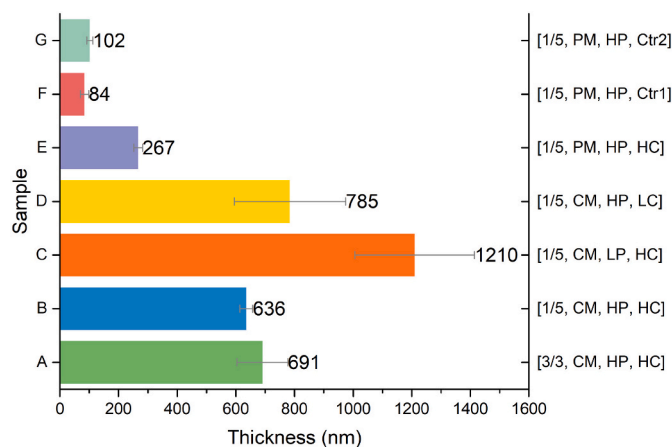


**Fig. 3.** Coating thickness of samples prepared at different deposition conditions. The right axis label shows the corresponding deposition condition in the form of [HMDSO flow rate/AgNO<sub>3</sub> flow rate, working mode, power, AgNO<sub>3</sub> concentration].

[16], and directly related to the physical properties of biomaterials. In this part of the work, the thickness of the coating deposited on a silicon wafer was measured and shown in Fig. 3.

A large variation of the thickness can be observed depending on the experimental conditions. It can be deduced that coatings under pulsed mode (sample E) have a lower thickness likely because of a scarce deposition during the OFF time. At low power for sample C coatings are more deposited at a high growth rate. This could be ascribed to a lower substrate heating likely leading to enhanced species adsorption.

Due to the complex surface morphology of the coatings which is described in Section 3.1.4, the coating thickness control is a complex task for aerosol-assisted plasma deposition which depends on varieties of experimental parameters. In addition to the experimental parameters (dissipated power, monomer flow rate, molecular weight) incorporated in the classical Yasuda formula [17], the coating growth can also be affected by aerosol droplet number density and their sizes.

Surface wettability can affect bacteria and cell adhesivity and conditions of cell proliferation [19]. The static water contact angle was measured as an indicator of the coating's wettability. Coatings deposited with silver nitrate aerosols shows the water contact angle in the range of 10° to 57°, as shown in Table 3, where sample C treated under LP has the most hydrophilic surfaces with WCA of 10°. Sample A deposited under HP exhibits the largest WCA of 57°. All deposited coating can be considered as hydrophilic, which is highly beneficial for biomedical applications as shown in Section 3.2.3. However, it should be noted that wettability depends on not only the chemical composition but also the surface morphology of the coatings [20]. Similar hydrophilic surfaces can be found for aerosol-assisted deposited deposition with ethylene and vancomycin/gentamicin, where surfaces are characterized with hydrophobic hydrocarbon groups and complicated morphology due to formation of nanocapsules [11,13]. In the following sections, complex surface morphology is observed for coatings deposited with AgNO<sub>3</sub> aerosols, which is studied by SEM techniques. Hydrocarbon functionalities are found for coating deposited with HMDSO by FTIR/XPS methods. Therefore, the measured WCA is a complex function of the chemical composition and surface morphology for the coatings deposited in this work.

#### 3.1.2. FTIR spectroscopy

The surface chemical structure in the deposited coatings was studied by FTIR spectroscopy in the range of 4000 cm<sup>-1</sup> to 400 cm<sup>-1</sup> and shown in Fig. 4. FTIR spectra were normalized to the peak intensity of Si-O-Si band in the range of 1010–1090 cm<sup>-1</sup>. A broad OH stretching band is also found centering at 3380 cm<sup>-1</sup> [21]. Absorption bands are

**Table 3**  
Water contact angle for samples deposited under different conditions.

Sample	A	B	C	D	E	F	G
WCA/°	57 ± 2	16 ± 3	10 ± 3	40 ± 5	44 ± 5	36 ± 9	54 ± 3

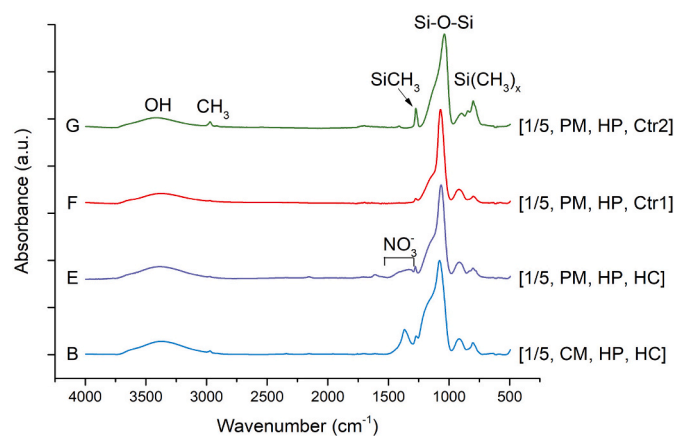


**Fig. 4.** FTIR spectra for samples at different deposition conditions. Samples A, C, D share similar FTIR spectra as sample B and are presented in Fig. S1 in the Supporting Information.

observed at  $2970\text{ cm}^{-1}$  for C–H asymmetric stretching vibrations in Si-CH<sub>3</sub> groups [21,22],  $1270\text{ cm}^{-1}$  for CH<sub>3</sub> deformation vibrations and symmetric bending in Si-CH<sub>3</sub> groups [21,23],  $850\text{ cm}^{-1}$  for Si–C stretching vibrations in Si-(CH<sub>3</sub>)<sub>3</sub> and  $800\text{ cm}^{-1}$  for CH<sub>3</sub> stretching vibrations and rocking vibrations in Si-(CH<sub>3</sub>)<sub>2</sub> groups [21,24]. These bands indicate retention of –CH<sub>3</sub> groups from HMDSO in the coating.  $1038\text{ cm}^{-1}$  and  $1068\text{ cm}^{-1}$  are assigned for Si–O–Si asymmetric stretching vibrations in Sample G and other samples, respectively. Compared with Si–O–Si band position for Sample G, where only HMDSO is introduced in the deposition, the Si–O–Si bands shifting to a higher wavenumber for other samples can be attributed to the higher amount of oxygen in the coatings [22]. The H<sub>2</sub>O and AgNO<sub>3</sub> from solution can be the sources of oxygen, which promotes the formation of Si–O–Si via oxidation reactions in the plasma deposition. Since the peak integral of Si-CH<sub>3</sub> at  $1270\text{ cm}^{-1}$  can serve as an index of bonds with carbon-containing groups [23,25], the organic content of the coating can be described by the ratio of the area between bands Si-CH<sub>3</sub> ( $1270\text{ cm}^{-1}$ ) and Si–O–Si ( $1038$  or  $1068\text{ cm}^{-1}$ ), as also used in the literature [22,23]. The peak of Si–O–Si can also be noticed in the FTIR spectra for sample E-FL1 and E-FL3 (see Fig. S5) which is also an indication of similarity between PM and CM deposition mode.

Comparing with the sample obtained with only HMDSO precursor (sample G), other samples show even higher inorganic properties with larger Si–O–Si peak integral, relative to Si-CH<sub>3</sub> peak integral. The relatively fewer methyl groups can also increase the surface wettability [20], which is related to the water contact angle measurements shown in the previous section. A broad NO<sub>3</sub><sup>–</sup> nitrate band is well detected in the range of  $1280\text{--}1520\text{ cm}^{-1}$  [21] for samples E and B, suggesting retention of AgNO<sub>3</sub> in the nanocapsules. It should be noted that sample G exhibits OH bands possibly because there is remaining water in the gas channel where aerosols can condense involved in the plasma polymerization, when no additional water is intentionally fed into discharge indicated in the experimental condition.

### 3.1.3. XPS

In order to get better insights into coating chemistry, XPS was used to quantitatively characterize the chemical constituents at the top layer of the coatings. Atomic contents determined from XPS survey spectra are presented in Table 4. A very low Ag content is found in sample D,

because of deposition from aerosol with a low AgNO<sub>3</sub> concentration. The main atomic elements found in samples F and G are C, O, Si, since HMDSO works as the precursor. However, a very small amount of Ag and N are also found on sample G, which can be negligible. This is possibly due to some remaining AgNO<sub>3</sub> solution in the atomizer channel.

As observed from the XPS results, the carbon, silicon, and oxygen atomic ratios of the considered samples are far from those of HMDSO deposition. In particular, the C/Si and O/Si ratio are, respectively, much lower and higher. Considering that carbon originates from the HMDSO and that the contribution of oxygen from possible silver oxide or nitrate can be supposed limited, the composition analysis indicates important oxidation of the HMDSO, due to the presence of water in the feed. This oxidation is likely responsible for the hydrophilic character of the coating. Concerning the silver content, as expected the Ag/Si atomic concentration ratio is higher for the coatings deposited at low power or in pulsed mode. This is due to the reduced activation of the HMDSO in the low power mode, leading to incomplete coverage of AgNO<sub>3</sub> droplets during the deposition. As for the pulsed mode case, that is because of important condensation of AgNO<sub>3</sub> aerosols on the substrate during the OFF time. Finally, considering that XPS cannot analyze depth higher than a few nanometers, it should be supposed that silver is not homogeneously covered by the silicone-like shell. Sample G shows a similar chemical composition as sample F deposited with water aerosols. This is probably due to the remaining water adsorbed in the gas channel and further transported to the discharge during the deposition for sample G. The reactive oxygen species formed from water can lead to an etching effect of sample surface, which explains the low carbon content in XPS measurement for sample G surface and, at the same time, high content of CH<sub>x</sub> groups in coating's bulk detected by FTIR. However, such etching effect is subtle and difficult to be observed by SEM as shown in Section 3.1.4.

### 3.1.4. SEM and EDX spectroscopy

The surface morphology of samples was checked by SEM as illustrated in Fig. 5. Fig. 5(G1, G2) shows that a flat coating on sample G is obtained by deposition only with the precursor of HMDSO and in the absence of aerosol. Injection of the H<sub>2</sub>O aerosol (sample F) also leads to an almost flat coating with only some defects as shown in Fig. 5(F1, F2). Palumbo and Lo Porto et al. [11,13] also reported the flat coating with H<sub>2</sub>O aerosol and emphasized the importance of solid solute to form the nanocapsules. When  $\mu\text{m}$  water aerosol droplets travel to the discharge zone, the discharge is slightly affected to form filaments to produce local strong fragmentation of HMDSO; thus some small particles or non-uniform deposited areas were observed on the coating. Both Fig. 5(A1, A2) of sample A and Fig. 5(B1, B2) of sample B show spherical features but with different surface morphology and particle density. In the latter case, more and bigger nanocapsules are present on the substrate, with regular spherical shapes. Obtained coating features are similar to the ones found in reference [12] and likely HMDSO polymerizes on the surface of the AgNO<sub>3</sub> solution droplets, freezing their shape. On the other hand, in Fig. 5(A1, A2) fewer and smaller nanocapsules are observed with irregular surfaces. This is due to the high HMDSO/AgNO<sub>3</sub> ratio: the lower aerosol solution flow rate causes easier evaporation of droplets from one side, whereas the high HMDSO flow rate leads to a higher polymer precursor density and in turn to the formation of irregular aggregates. Similarly, in the case of the PM deposition, SEM imaging of the samples E-FL1 and E-FL3 in Fig. S6 also shows that larger particles were formed in the coating on sample E-FL1.

**Table 4**  
Results of XPS measurements of atomic composition for samples A–G.

Sample	C1s/at.%	N1s/at.%	O1s/at.%	Si2p/at.%	Ag3d/at.%	Ag/Si
A	21.8 ± 1.3	1.8 ± 0.9	50.3 ± 3.5	23.2 ± 0.2	2.9 ± 1.4	0.13
B	14.4 ± 1.6	1.3 ± 0.5	57.4 ± 1.0	24.3 ± 1.2	2.5 ± 0.6	0.10
C	20.8 ± 1.6	0.7 ± 0.7	52.9 ± 0.3	21.3 ± 0.2	4.3 ± 0.5	0.38
D	4.6 ± 0.6	0.3 ± 0	66.9 ± 0.5	28.1 ± 0.2	0.1 ± 0.1	0.00
E	46.8 ± 2.2	0.3 ± 0.2	35.1 ± 1.5	13.0 ± 0.1	5.0 ± 0.3	0.38
F	7.7 ± 0.8	0.7 ± 0	63.5 ± 0.3	28.0 ± 1.1	0.1 ± 0.1	0.00
G	6.6 ± 0.4	0.2 ± 0.2	64.0 ± 0.3	28.2 ± 0.1	0	0.00

In samples where low polymerization is expected due to the use of low power and pulsed mode, i.e. Fig. 5(C1, C2) of sample C and Fig. 5(E1, E2) of sample E, due to the use of low power and pulsed mode respectively, a more complex and irregular morphology can be observed. In sample C the polymerization of the monomer is probably not high enough to always allow good coverage of the droplets before their evaporation. Sample E was deposited in pulsed mode discharge: during the OFF time the polymerization slows down substantially, while the flow of the two aerosol remains unaltered, leading to more irregular deposition. In Fig. 5(D1, D2) of sample D, where a low concentration of AgNO<sub>3</sub> was used, a similar surface morphology to Fig. 5(B1, B2) can be observed but with smaller and fewer nanocapsules.

The coating formation was further examined by SEM at the cross-sections of samples. We present the cross-sections of samples A and B in Fig. 6. Both cross-section SEM images show that coatings consist of a layer of a polymeric matrix with nanocapsules embedded inside and grafted on the surface.

To further validate the compositional distribution and nanostructure of the coating, EDX was employed for the surfaces of sample B at continuous mode and sample E deposited in pulsed mode. In order to avoid the interference from the silicon substrate when trying to detect the Si spatial distribution from the coating, a polycarbonate substrate was used, instead, during the sample deposition for EDX analysis. Fig. S2 illustrates the Si and Ag EDX maps and global spectrum and chemical analysis, together with the corresponding SEM image of the coating B. Si was introduced due to fragmentation of HMDSO and involved the matrix formation [24]. A uniform distribution can be observed at the EDX Si map in Fig. S2(b), revealing that the organosilicon matrix forms on the substrate and also covers the aerosol droplets. Very interestingly, the EDX map of Ag in Fig. S2(c) highlights the scattered distribution of Ag element, which situates mostly in the position of the spherical structures (compare with Fig. S2(a)). This core-shell structure has also been witnessed and confirmed in the work of Lo Porto et al. for the deposition of vancomycin [11].

As also presented in the supporting information, Fig. S3(a) reveals the surface morphology of sample E obtained under pulsed mode. From the chemical composition analysis, we can observe that the silver content in the coating is higher for the pulsed mode deposited one. The relatively high Ag content in sample E is attributed to the continuous condensation of AgNO<sub>3</sub> aerosols in the OFF time when HMDSO polymerization does not occur. Similar to Fig. S2(b), Fig. S3(b) also presents a quasi-uniform Si element distribution. Nonetheless, the Ag element distribution in Fig. S3(c) exhibits a diffuse distribution in the volume, when compared to the size of nanocapsules in Fig. S3(a), which is different from that of continuous mode.

### 3.1.5. The hypothesis of deposition mechanisms

The hypothesis of the mechanism behind deposition Ag-containing coating by AAPPD can be proposed based on the above-mentioned results. Fig. S4 presents the three stages (a–c) of Ag-containing coating deposition. In the first stage (a), aerosol droplets containing AgNO<sub>3</sub> are transported by helium gas flow into the chamber, while HMDSO aerosols evaporate completely before entering the plasma zone, due to its high volatility and resulting in no nanocapsules formation in the

coating (see Fig. 5(G1, G2)). Strong gas heating is noticed in atmospheric pressure discharge due to the high-frequency collisions, which can lead to a gradual decrease in the droplet size due to the evaporation of the aerosol. The gas heating is confirmed by the observation of PET film deformation under continuous discharge mode with an estimated sample temperature slightly below the glass transition temperature of 350 K. In the second stage (b), HMDSO and H<sub>2</sub>O vapor are efficiently fragmented and polymerization processes start on the substrate as well as on the surface of AgNO<sub>3</sub>-containing droplets. Meanwhile, AgNO<sub>3</sub> aerosol droplets are continuously evaporated and transported to the substrate due to sedimentation and diffusion. This results in the formation of the nanocapsules (Fig. 5, samples A–E) covered by the polymeric matrix. The processes are also confirmed by EDX results where a core-shell structure with Ag in the core and polymer shell was observed. In the third stage (c), the polymerization continues on the substrate and AgNO<sub>3</sub> aerosol droplets surface, to embed the nanocapsules inside the coating, which has been proven by the cross-section images of samples B and E (Fig. 6). As the polymerization proceeds, neighboring nanocapsules grow in size and start to connect and intersect. The intersection of nanocapsules can be confirmed with the detection of surface morphology in Fig. 5 for samples A–E, especially in Fig. 5(B1–B2). As for the pulsed mode deposition, in the ON time, the deposition continues similar to the above-described process. In the OFF time, the AgNO<sub>3</sub> aerosol droplets condensate on the substrate and form a layer; then they spread on the surface and lose their spherical shapes without the confinement by HMDSO polymerization. These two processes alternate and contribute to forming the more complex morphology and smaller nanocapsules than CM mode deposition, where smaller-sized nanocapsules can be attributed to low HMDSO polymerization. Indeed, such an effect is confirmed by the comparison of the surface morphology for the samples treated in continuous mode (Fig. 5(B1, B2)) versus pulsed mode (Fig. 5(E1, E2)).

### 3.2. Antibacterial properties

To explore the potential application of the aerosol assisted-plasma deposition for antibacterial coating, PET films were employed as substrates due to the excellent mechanical strength and good chemical stability [26,27]. Owing to the mild gas temperature for the treatment of PET films and high Ag content for antibacterial efficiency, pulsed mode was chosen to study the deposition on PET films. High power and AgNO<sub>3</sub> concentration were also favored because of strong polymerization and high Ag content. In order to control the Ag<sup>+</sup> ions released from the coating, the HMDSO/AgNO<sub>3</sub> aerosol gas flow ratio was adjusted as shown in Table 2. It is expected that pulsed mode of the deposition on PET film follows the same trends as continuous mode of the deposition on Si wafer, though there may be a difference in deposition between PET film and Si wafer mainly due to the thickness of the substrate and its dielectric constant. The WCA results of sample E-FL1 and E-FL3 are shown in Table S1. As expected, lower aerosol flow ratio of HMDSO/AgNO<sub>3</sub> used to preparesample E-FL1 exhibits higher Ag content than E-FL3, see XPS results in Table S2. The ratio of Ag/Si for both coatings can represent the relative content of Ag despite of possible contamination of the sample's surface by carbon. Therefore, we can conclude that Ag

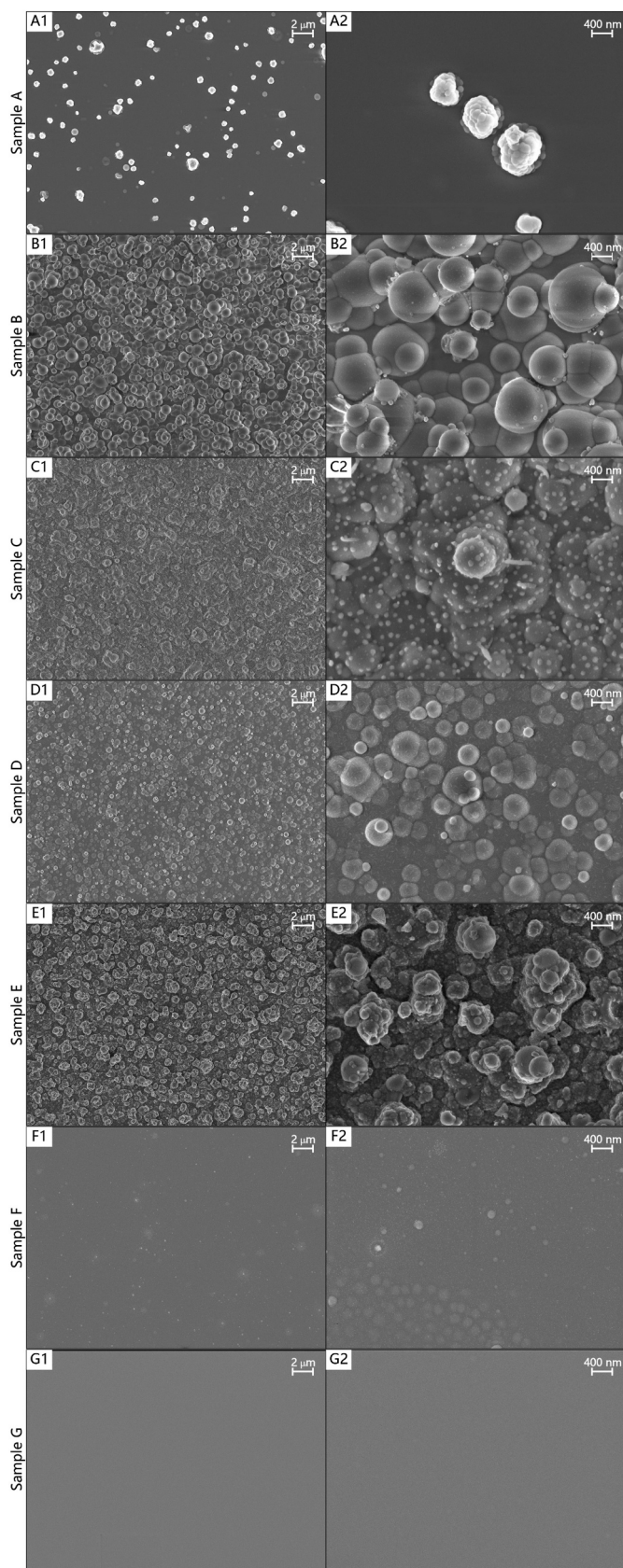


Fig. 5. SEM images under 10k  $\times$  magnification (A1, B1, C1, D1, E1, F1, G1) and 50k  $\times$  magnification (A2, B2, C2, D2, E2, F2, G2) of samples A–G deposited with AAPPD for 10 min.

content in the coating can be adjusted for both CM and PM deposition by varying the aerosol flow ratio of HMDSO/AgNO<sub>3</sub>. SEM imaging of the samples prepared in PM deposition (see Fig. S6) shares the same trend as in CM deposition (see Fig. 5) and the morphology of the samples surface can be strongly modified by varying the aerosol flow ratio. AFM imaging was also performed for sample E-FL1 and E-FL3. The results (see Fig. S7) demonstrate that the surface of sample E-FL1 has larger roughness than E-FL3. Higher surface area (higher roughness) of the coatings on sample E-FL1 should promote the release of silver. In the following sections, ion release measurements, antibacterial tests, and cytotoxicity assay were performed to investigate the antibacterial performance of the coatings.

### 3.2.1. Ag<sup>+</sup> ion release

The biocidal effects of Ag-embedded coatings directly depend on the release of Ag<sup>+</sup> ions. The Ag<sup>+</sup> ion release rate was measured by ICP-MS. Fig. 7 shows the cumulatively released Ag<sup>+</sup> from deposited PET films. When comparing different samples, E-FL1 shows a higher amount of Ag<sup>+</sup> release than E-FL2 and E-FL3. It is related to the higher content of Ag in the E-FL1 coating, see Supporting Materials Table S2, as well as to more developed surface with large surface area as shown by AFM imaging, Fig. S7. The controlled sample (G-FL5) rarely demonstrate ion release because AgNO<sub>3</sub> aerosol was excluded in the deposition. The higher the amount of AgNO<sub>3</sub> aerosol, the higher amount of Ag is deposited in the coating and further can be released. This release can take place through the small localized pores and cracks in the barrier layer formed by polymerized HMDSO [28]. The hydrophilic surface of the coatings was also beneficial for the water penetration through the coating resulting in more effective Ag<sup>+</sup> release. Meanwhile, as the amount of HMDSO increases from E-FL1 to E-FL3, an increasingly thicker barrier is created against release. The increase of barrier layer thickness can suppress the release of Ag<sup>+</sup> ions. It is necessary to mention that there is two-phase release kinetics for all deposited samples. A fast release of Ag<sup>+</sup> ion is observed on the first day for E-FL1, E-FL2, and E-FL3, afterward followed by a slower Ag<sup>+</sup> ion release. The initial fast release ensures antibacterial protection for an early post-operation period which is the most essential stage for infection risk [1]. The initial burst release of Ag<sup>+</sup> can be attributed to the Ag nearest to the surface in the coating. Especially for the pulsed mode deposition, many nanocapsules with a thinner shell cannot effectively block the Ag<sup>+</sup> diffusion into an aqueous environment. Whereas the Ag embedded deeply in the coating and in the nanocapsules with a thicker shell can be the reason for the long-term slow release.

The release kinetics can be further investigated by using Korsmeyer-Peppas model expressed in Eq. (1) [29,30]:

$$\frac{M_t}{M_\infty} = kt^n \quad (1)$$

where  $M_t$  is the released antibacterial agent at time  $t$ ;  $M_\infty$  is the total amount of released antibacterial agent;  $k$  is the release rate constant depending on the structural and geometric feature of polymeric matrix;  $n$  is the release exponent related to the release mechanism of antibacterial agent.  $n < 0.5$  denotes a quasi-Fickian diffusion;  $n = 0.5$  corresponds Fickian diffusion;  $0.5 < n < 1$  is anomalous diffusion;  $n > 1$  means a Case II diffusion [31]. The Korsmeyer-Peppas equation can be applied to fit the release curve to determine the type of release mechanism. This equation has been reported to describe drug release from plasma polymers in literature [32,33]. In our case, the release curve for sample E-FL1 is fitted to get  $n = 0.12$  with a correlation coefficient of 0.999. This confirms that Korsmeyer-Peppas model is suitable to describe release of Ag<sup>+</sup> ions from the coating and shows that the release mechanism of this core-shell structured Ag-containing coating can be explained by the quasi-Fickian diffusion [34]. The low value of release exponent  $n$  is possibly due to the morphology of nanocapsules, since the release exponent  $n$  is around 0.5 for layer-structure antibacterial coating with plasma polymers [32,33]. Considering

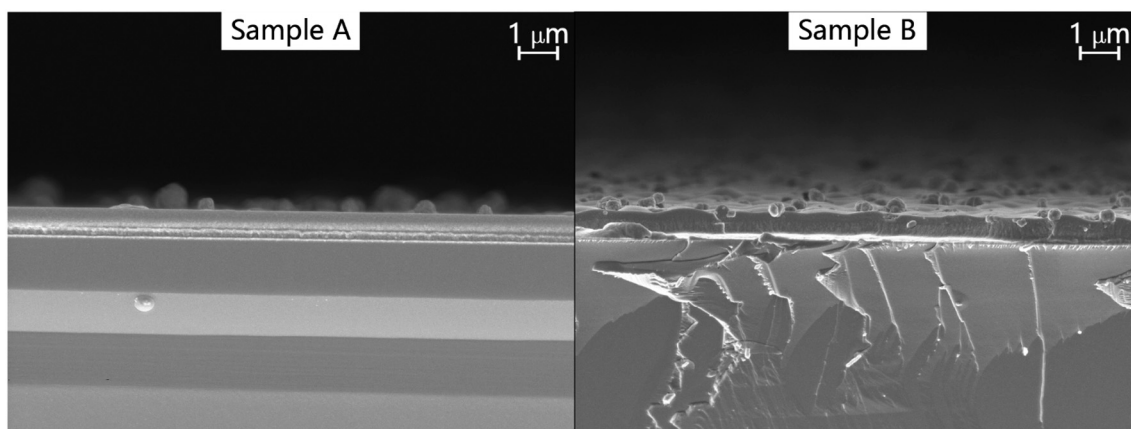


Fig. 6. SEM images of the cross-sections for samples A and B at a magnification of  $20\times$ .

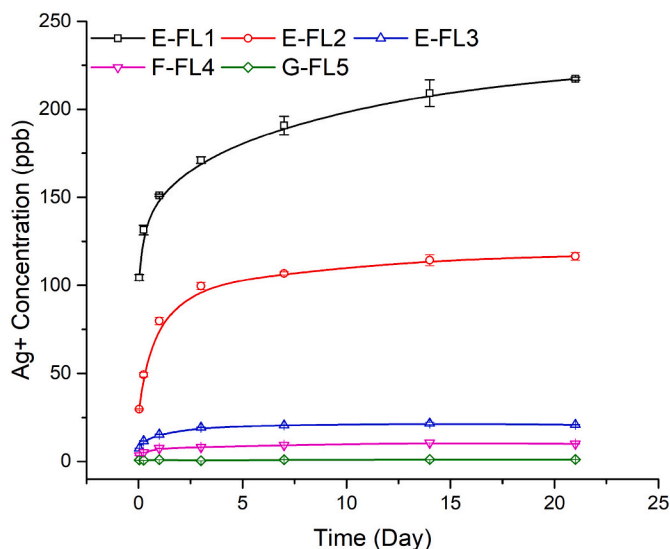


Fig. 7.  $\text{Ag}^+$  ion cumulatively released from deposited coatings on PET films at different experimental conditions.

the constraint of  $M_t/M_\infty < 0.6$  in the Korsmeyer-Peppas model [31], for the samples E-FL2 and E-FL3, release curves can be fitted with  $n < 0.3$  and lower correlation coefficients. Similar release mechanisms by quasi-Fickian diffusion are also expected due to similar coating structures to the sample E-FL1.

For different samples, the release rate can be adjusted by controlling the HMDSO/ $\text{AgNO}_3$  flow ratio.  $\text{Ag}$ -containing coatings show release time longer than 21 days, showing the potential for long-term  $\text{Ag}^+$  agent release. The long-term release is also needed for maintaining antibacterial properties in revision or second surgery where infections are often already found, and for near-patient environmental surfaces [35,36]. In literature, there is a well-defined minimum  $\text{Ag}^+$  concentration of 0.1 ppb that exhibits inhibition of bacteria growth [37]. An excessive amount of  $\text{Ag}^+$  release in an aqueous physiological environment often associated with side effects and cytotoxicity. Harges et al. reported  $\text{Ag}^+$  concentration in human blood lower than 56.4 ppb to be non-cytotoxic [38]. It is important to emphasize that the released  $\text{Ag}^+$  from optimized sample E-FL3 is 25 ppb after 21 days, which seems to have the potential to be biocompatible. Both antibacterial tests and cytotoxicity assay were further performed in the following sections to examine the bactericidal effects and cell viability of the coatings.

### 3.2.2. Antibacterial tests

Antibacterial properties of coating surfaces were tested on two

different bacterial strains: *E. coli* and *S. aureus*. *E. coli* and *S. aureus* are representative of Gram-negative and Gram-positive bacteria [39,40], respectively. The viability of bacteria exposed to samples was evaluated by two methods: standard plate count method and through the changes of metabolic activity (XTT assay). XTT assay shows high sensitivity and dynamic ranges, which has been applied to study the vitality of bacteria [42,43].

Fig. 8(a) shows the reduction of colonies for both tested bacteria after exposure to coated samples. F-FL4 and G-FL5 manifest almost no reduction of bacteria colonies. While starting from E-FL3 to E-FL1, the bacteria colonies after incubation are drastically decreased, which can be attributed to more released  $\text{Ag}^+$  ions. Sample E-FL3 shows an effective antibacterial activity by witnessing a log reduction of colony-forming unit 2.55 and 0.44 for *E. coli* and *S. aureus*, respectively. Compared with samples culturing with *S. aureus*, stronger bactericidal effects are found for *E. coli*, which was also observed by other researchers [28,44]. This phenomenon is caused by the thicker cell walls in Gram-positive bacteria than those in Gram-negative bacteria, which prevent cells from penetration of  $\text{Ag}^+$  ions into the cytoplasm and cell lysis [44,45]. Fig. 8(b) illustrates the metabolic activity of *E. coli* and *S. aureus* during the tests. The control in the XTT assay was conducted with the addition of uncoated PET films. Control samples show high metabolic activity as expected. After culturing films with *E. coli* and *S. aureus*, E-FL1 shows the strongest suppression of bacteria activity, followed by E-FL2 and E-FL3. While F-FL4 and G-FL5, deposited without  $\text{AgNO}_3$ , aerosol present no suppression of bacteria activity. It, hence, confirms the antibacterial activity of the composite coating, depending on the amount of  $\text{Ag}^+$  ion released from films. The sample E-FL3 already shows the reduction in bacteria after immersion for 1 day with 15 ppb  $\text{Ag}^+$  release. A higher amount of  $\text{Ag}^+$  released from E-FL1 of 151 ppb and E-FL2 of 80 ppb (Fig. 7) results in a stronger antibacterial effect, as confirmed by the reduction of bacteria colonies and metabolic activity in Fig. 8. Swathy et al. have reported a similar level of around 50 ppb of  $\text{Ag}^+$  released from AgNPs to cause antibacterial activity [46]. Many possible mechanisms are leading to the bactericidal effects of  $\text{Ag}^+$ , including binding to the cell membrane to induce cell lysis, binding to DNA to prevent replication, binding to proteins/enzymes to suppress bacterial metabolism [47]. The bacterial cell membrane also has a negative charge promoting the electrostatic interaction with positively charged  $\text{Ag}^+$  to enhance the antibacterial effects [48]. The exact mechanism realized in studied samples and leading to bacteria-killing was not yet investigated and needs to be clarified in the future, but this is out of the scope of this work. Although  $\text{Ag}$  loaded samples have proven their antibacterial efficacy, in order to use these coatings for biomedical applications, the biocompatibility needs to be examined by cell viability assay especially for the samples with a higher amount of  $\text{Ag}^+$  release which can be lethal to the cells.

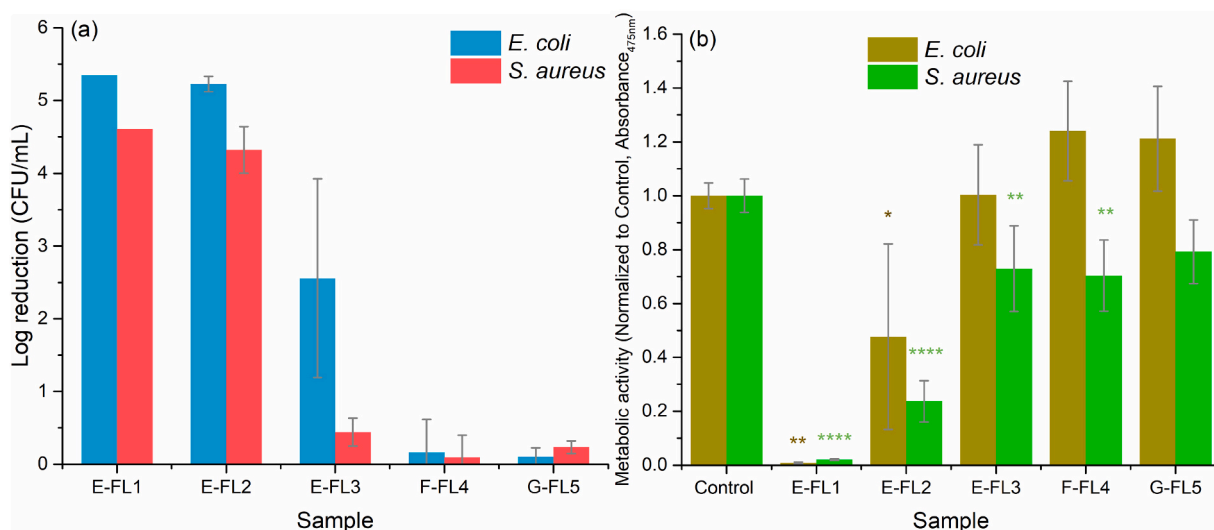


**Fig. 8.** Antibacterial activity of sample FL1–FL5, expressed as (a) CFU/ml log reduction; (b) metabolic activity, measured with XTT assay. Data are shown as the mean value  $\pm$  standard deviation. One-way ANOVA followed by Dunnett's test is applied for determination of statistical significance with \* $p < 0.01$ , \*\* $p < 0.01$ , \*\*\* $p < 0.0001$ . The control denotes the bacteria cultured with the untreated film. The metabolic activities for both bacteria are normalized to their controlled groups.

### 3.2.3. Cytotoxicity assay

Cytotoxicity was studied through confocal microscopy analysis and cell viability of murine fibroblasts incubated with sample. Murine fibroblasts have been used to study the in vitro cytotoxicity in many experiments [49–51]. When considering these coatings for medical applications, the cytocompatibility or low cytotoxicity is required for antibacterial coatings in contact with cells. There are two control samples: cells incubated under standard protocol, using unexposed medium in order to follow the growth of cells (ctrl 2) and cells incubated with untreated PET films at the same condition (ctrl 1). Fig. 9(a) shows the cells cultured with the unexposed medium. Cell proliferation PET films without treatment (see Fig. 9(b)), revealing that PET films itself do not influence the viability of cells.

When using sample G-FL5 treated only with HMDSO, and F-FL4 deposited with a mixture of HMDSO and H<sub>2</sub>O aerosol, the confocal microscopy analyses manifest a normal living state of cells, which are

presented in Fig. 9(g, f). This indicates the non-cytotoxicity of coating made from HMDSO precursor and mixture with H<sub>2</sub>O aerosol. However, comparing with the above-mentioned results, a strong contrast is found in Fig. 9(c, d), where cells were incubated with samples E-FL1 and E-FL2. Both samples were prepared at high AgNO<sub>3</sub> aerosol flow injection into the reactor, leading to the excessive Ag<sup>+</sup> ion release from the coatings, resulting in high cytotoxicity to fibroblast cells. The proposed method provides precise and simple control over Ag<sup>+</sup> release from the coatings and so in cytotoxicity by reducing the AgNO<sub>3</sub> aerosol flow rate. Indeed, sample E-FL3 prepared in an optimized condition was characterized by the very low cytotoxicity to cells as shown in Fig. 9(e).

Cell viability was further investigated by quantitative analysis, shown in Fig. 10. After 2 h, high cytotoxicity is already detected for cells in contact with E-FL1, while E-FL2 showed lower cytotoxic effects. After 1 day of incubation, cells are almost completely killed after exposure to E-FL1 and E-FL2. After 2 days, cell viability reaches a stable

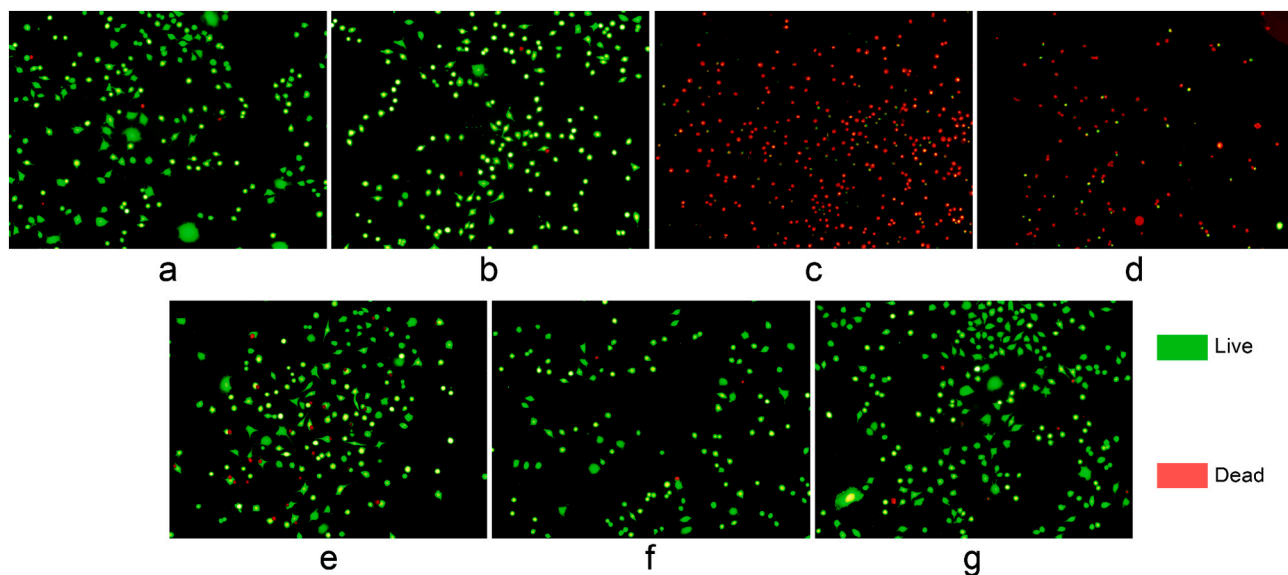


**Fig. 9.** Confocal microscopy analysis of (a) ctrl 1: cells only; (b) ctrl 2: cells incubated with untreated PET film; (c) cells incubated with E-FL1; (d) cells incubated with E-FL2; (e) cells incubated with E-FL3; (f) cells incubated with F-FL4; (g) cells incubated with G-FL5; Cells dyed as green and red are alive and dead, respectively. (For interpretation of the references to color in this figure legend, the reader is referred to the web version of this article.)

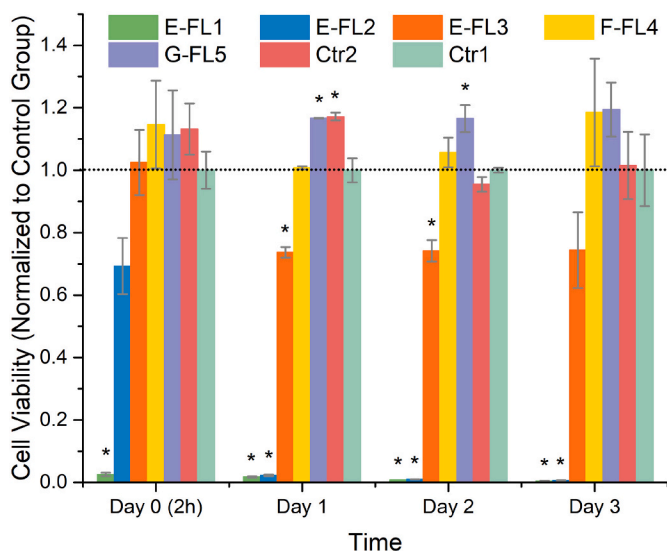


Fig. 10. Cell viability measured after 2 h, 24 h, 48 h, and 72 h of incubation with sample FL1-FL5. Data are shown as the mean value  $\pm$  standard deviation. One-way ANOVA followed by Dunnett's test; \* $p < 0.05$ .

state for these 7 samples. Sample E-FL3 has shown the viability higher than 70% associated with antibacterial activity with a CFU log reduction of 2.55 and 0.44 for *E. coli* and *S. aureus*, respectively. This can be considered as biocompatible antibacterial coating according to ISO 10993-5 standard. The mechanism of  $\text{Ag}^+$  cytotoxicity on cells is believed to be the interaction of  $\text{Ag}^+$  with cell respiratory enzyme system that induces the generation of reactive oxygen species, further cause protein denaturation, DNA damage, and cell apoptosis [52]. Sample E-FL1 releases 110 ppb  $\text{Ag}^+$  after 2 h causing strong cytotoxicity to fibroblast cells, while sample E-FL2 releases 34 ppb  $\text{Ag}^+$  after 2 h and can be regarded as biocompatible due to the remaining cell viability of 70%. At long exposure E-FL2 becomes cytotoxic by releasing more  $\text{Ag}^+$  ions. Therefore, 34 ppb  $\text{Ag}^+$  can be regarded as the maximum allowed  $\text{Ag}^+$  concentration for this kind of biocompatible coating. This concentration level can also be supported by the 25 ppb of  $\text{Ag}^+$  released from biocompatible coating E-FL3 after 3 days. Similar cytotoxicity level was also found for 39.4 ppb  $\text{Ag}^+$  released from carbon-encapsulated Ag (Ag@C) nanoparticles by Yan et al. [53].

#### 4. Conclusions

Antibacterial Ag-containing composite coatings were synthesized through a one-step aerosol-assisted atmospheric pressure plasma process for biomedical applications. It was shown that surface morphology and chemical composition of the coatings can be tuned by varying the experimental parameters: power,  $\text{AgNO}_3$  concentration, aerosol flow ratio, discharge mode. The formed Ag-containing nanocapsules in the coating under continuous mode of deposition had a structure with  $\text{AgNO}_3$  in the core coated by an organosilicon shell. HMDSO/ $\text{AgNO}_3$  aerosol flow ratio was varied to produce a coating with different thicknesses of the HMDSO barrier layer and Ag content in the nanocapsules and to achieve the controlled release of  $\text{Ag}^+$ . A two-phase  $\text{Ag}^+$  ion release kinetics was observed for treated PET films, which is beneficial to maintain antibacterial activity in medical care not only in the early stage of an application but through a long period. The  $\text{Ag}^+$  ions experienced a fast release during the first 24 h followed by a relatively long-term release of more than 21 days. Antibacterial tests performed with *E. coli* and *S. aureus* and cytotoxicity analyzed with murine fibroblasts were used to investigate the bio-applicability of antibacterial coatings. Results revealed that antibacterial activity and cytotoxicity can be controlled by variation of the aerosol flow ratio. The coatings

were capable to provide a log reduction of CFU 2.55 and 0.44 for *E. coli* and *S. aureus*, respectively with low cytotoxicity. The antibacterial coatings prepared by aerosol-assisted plasma deposition shed light on possible medical applications such as wound dressings, catheters, and near-patient environmental surfaces, where antibacterial properties are required with controlled release and low cytotoxicity.

#### CRedit authorship contribution statement

**Lei Wang:** Writing - original draft, Investigation. **Chiara Lo Porto:** Writing - review & editing, Investigation. **Fabio Palumbo:** Writing - review & editing, Methodology. **Martina Modic:** Writing - review & editing, Investigation. **Uroš Cvelbar:** Supervision. **Rouba Ghobeira:** Investigation. **Nathalie De Geyter:** Supervision. **Mike De Vrieze:** Investigation. **Špela Kos:** Investigation. **Gregor Serša:** Investigation. **Christophe Leys:** Funding acquisition, Supervision. **Anton Nikiforov:** Writing - review & editing, Conceptualization, Supervision.

#### Declaration of competing interest

The authors declare that they have no known competing financial interests or personal relationships that could have appeared to influence the work reported in this paper.

#### Acknowledgments

This work was supported by the China Scholarship Council (File No. 201503170253) and co-funding of Ghent University (Reference Code: DOZA/DDC/AM/006b-2016). The work was partially funded by the M Era-Net program, project "PlasmaTex", COST (European Cooperation in Science and Technology) AMiCi Action CA15114, and FWO/ARRS agencies project number G084917N and N3-0056.

#### Appendix A. Supplementary data

Supplementary data to this article can be found online at <https://doi.org/10.1016/j.msec.2020.111496>.

#### References

- [1] M. Cloutier, D. Mantovani, F. Rosei, Antibacterial coatings: challenges, perspectives, and opportunities, Trends Biotechnol. 33 (2015) 637–652, <https://doi.org/10.1016/j.tibtech.2015.09.002>.
- [2] Z. Zhang, V.E. Wagner, J.C. Victor, Antimicrobial modifications on critical care implants, Antimicrob. Coatings Modif. Med. Devices, Springer International Publishing, Cham, 2017, pp. 1–36, [https://doi.org/10.1007/978-3-319-57494-3\\_1](https://doi.org/10.1007/978-3-319-57494-3_1).
- [3] Z. Geng, R. Wang, X. Zhuo, Z. Li, Y. Huang, L. Ma, Z. Cui, S. Zhu, Y. Liang, Y. Liu, H. Bao, X. Li, Q. Huo, Z. Liu, X. Yang, Incorporation of silver and strontium in hydroxyapatite coating on titanium surface for enhanced antibacterial and biological properties, Mater. Sci. Eng. C 71 (2017) 852–861, <https://doi.org/10.1016/j.msec.2016.10.079>.
- [4] X. Li, B. Wu, H. Chen, K. Nan, Y. Jin, L. Sun, B. Wang, Recent developments in smart antibacterial surfaces to inhibit biofilm formation and bacterial infections, J. Mater. Chem. B 6 (2018) 4274–4292, <https://doi.org/10.1039/C8TB01245H>.
- [5] J.A. Lemire, J.J. Harrison, R.J. Turner, Antimicrobial activity of metals: mechanisms, molecular targets and applications, Nat. Rev. Microbiol. 11 (2013) 371–384, <https://doi.org/10.1038/nrmicro3028>.
- [6] X.-F. Zhang, Z.-G. Liu, W. Shen, S. Gurunathan, Silver nanoparticles: synthesis, characterization, properties, applications, and therapeutic approaches, Int. J. Mol. Sci. 17 (2016) 1534, <https://doi.org/10.3390/ijms17091534>.
- [7] J. Kratochvíl, A. Kuzminova, O. Kylián, State-of-the-art, and perspectives of, silver/plasma polymer antibacterial nanocomposites, Antibiotics. 7 (2018) 78, <https://doi.org/10.3390/antibiotics7030078>.
- [8] F. Palumbo, G. Camporeale, Y.-W. Yang, J.-S. Wu, E. Sardella, G. Dilecce, C.D. Calvano, L. Quintieri, L. Caputo, F. Baruzzi, P. Favia, Direct plasma deposition of lysozyme-embedded bio-composite thin films, Plasma Process. Polym. 12 (2015) 1302–1310, <https://doi.org/10.1002/ppap.201500039>.
- [9] C.-P. Hsiao, C.-C. Wu, Y.-H. Liu, Y.-W. Yang, Y.-C. Cheng, F. Palumbo, G. Camporeale, P. Favia, J.-S. Wu, Aerosol-assisted plasma deposition of bio-composite coatings: investigation of processing conditions on coating properties, IEEE Trans. Plasma Sci. 44 (2016) 3091–3098, <https://doi.org/10.1109/TPS.2016.2591721>.

- [10] C. Lo Porto, F. Palumbo, F. Fracassi, G. Barucca, P. Favia, On the formation of nanocapsules in aerosol-assisted atmospheric-pressure plasma, *Plasma Process. Polym.* 16 (2019) 1900116, <https://doi.org/10.1002/ppap.201900116>.
- [11] C. Lo Porto, F. Palumbo, J. Buxadera-Palomero, C. Canal, P. Jelinek, L. Zajickova, P. Favia, On the plasma deposition of vancomycin-containing nano-capsules for drug-delivery applications, *Plasma Process. Polym.* 15 (2018) 1700232, <https://doi.org/10.1002/ppap.201700232>.
- [12] C. Lo Porto, F. Palumbo, G. Palazzo, P. Favia, Direct plasma synthesis of nano-capsules loaded with antibiotics, *Polym. Chem.* 8 (2017) 1746–1749, <https://doi.org/10.1039/C7PY00103G>.
- [13] F. Palumbo, A. Treglia, C. Lo Porto, F. Fracassi, F. Baruzzi, G. Frache, D. El Assad, B.R. Pistillo, P. Favia, Plasma-deposited nanocapsules containing coatings for drug delivery applications, *ACS Appl. Mater. Interfaces* 10 (2018) 35516–35525, <https://doi.org/10.1021/acsmi.8b11504>.
- [14] P.B. Flynn, S. Higginbotham, N.H. Alshraideh, S.P. Gorman, W.G. Graham, B.F. Gilmore, Bactericidal efficacy of atmospheric pressure non-thermal plasma (APNTP) against the ESKAPE pathogens, *Int. J. Antimicrob. Agents* 46 (2015) 101–107, <https://doi.org/10.1016/j.ijantimicag.2015.02.026>.
- [15] M. Modic, J. Kovač, J.R. Nicholls, Š. Kos, G. Serša, U. Cvelbar, J.L. Walsh, Targeted plasma functionalization of titanium inhibits polymicrobial biofilm recolonization and stimulates cell function, *Appl. Surf. Sci.* 487 (2019) 1176–1188, <https://doi.org/10.1016/j.apsusc.2019.05.153>.
- [16] P.M. Martin, *Handbook of Deposition Technologies for Films and Coatings: Science, Applications and Technology*, 3rd ed., William Andrew, 2009.
- [17] H.K. Yasuda, Some important aspects of plasma polymerization, *Plasma Process. Polym.* 2 (2005) 293–304, <https://doi.org/10.1002/ppap.200400071>.
- [18] Y. Arima, H. Iwata, Effect of wettability and surface functional groups on protein adsorption and cell adhesion using well-defined mixed self-assembled monolayers, *Biomaterials* 28 (2007) 3074–3082, <https://doi.org/10.1016/j.biomaterials.2007.03.013>.
- [19] P. Dimitrakellis, E. Gogolides, Hydrophobic and superhydrophobic surfaces fabricated using atmospheric pressure cold plasma technology: a review, *Adv. Colloid Interf. Sci.* 254 (2018) 1–21, <https://doi.org/10.1016/j.cis.2018.03.009>.
- [20] G. Socrates, G. Sokrates, *Infrared and Raman Characteristic Group Frequencies: Tables and Charts*, 3rd ed., John Wiley & Sons, 2004.
- [21] X. Deng, A.Y. Nikiforov, N. De Geyter, R. Morent, C. Leys, Deposition of a TMDSO-based film by a non-equilibrium atmospheric pressure DC plasma jet, *Plasma Process. Polym.* 10 (2013) 641–648, <https://doi.org/10.1002/ppap.201200166>.
- [22] R.A. Siliprandi, S. Zanini, E. Grimaldi, F.S. Fumagalli, R. Barni, C. Riccardi, Atmospheric pressure plasma discharge for polysiloxane thin films deposition and comparison with low pressure process, *Plasma Chem. Plasma Process.* 31 (2011) 353–372, <https://doi.org/10.1007/s11090-011-9286-3>.
- [23] R. Morent, N. De Geyter, S. Van Vlierberghe, P. Dubruel, C. Leys, L. Gengembre, E. Schacht, E. Payen, Deposition of HMDSO-based coatings on PET substrates using an atmospheric pressure dielectric barrier discharge, *Prog. Org. Coat.* 64 (2009) 304–310, <https://doi.org/10.1016/j.porgcoat.2008.07.030>.
- [24] M. Deilmann, M. Grabowski, S. Theiß, N. Bibinov, P. Awakowicz, Permeation mechanisms of pulsed microwave plasma deposited silicon oxide films for food packaging applications, *J. Phys. D: Appl. Phys.* 41 (2008) 135207, <https://doi.org/10.1088/0022-3727/41/13/135207>.
- [25] Y. Liu, C. Su, X. Ren, C. Fan, W. Zhou, F. Wang, W. Ding, Experimental study on surface modification of PET films under bipolar nanosecond-pulse dielectric barrier discharge in atmospheric air, *Appl. Surf. Sci.* 313 (2014) 53–59, <https://doi.org/10.1016/j.apsusc.2014.05.129>.
- [26] S. Nazari Pour, S.V. Ghugare, R. Wiens, K. Gough, S. Liu, Controlled *in situ* formation of polyacrylamide hydrogel on PET surface via SI-ARGET-ATRP for wound dressings, *Appl. Surf. Sci.* 349 (2015) 695–704, <https://doi.org/10.1016/j.apsusc.2015.04.181>.
- [27] X. Deng, C. Leys, D. Vujosevic, V. Vuksanovic, U. Cvelbar, N. De Geyter, R. Morent, A. Nikiforov, Engineering of composite organosilicon thin films with embedded silver nanoparticles via atmospheric pressure plasma process for antibacterial activity, *Plasma Process. Polym.* 11 (2014) 921–930, <https://doi.org/10.1002/ppap.201400042>.
- [28] R.W. Kormsmeier, R. Gurny, E. Doelker, P. Buri, N.A. Peppas, Mechanisms of solute release from porous hydrophilic polymers, *Int. J. Pharm.* 15 (1983) 25–35, [https://doi.org/10.1016/0378-5173\(83\)90064-9](https://doi.org/10.1016/0378-5173(83)90064-9).
- [29] N.A. Peppas, *Analysis of Fickian and non-Fickian drug release from polymers*, *Pharm. Acta Helv.* 60 (4) (1985) 110–111.
- [30] D.Y. Ariffin, L.Y. Lee, C.-H. Wang, Mathematical modeling and simulation of drug release from microspheres: implications to drug delivery systems, *Adv. Drug Deliv. Rev.* 58 (2006) 1274–1325, <https://doi.org/10.1016/j.addr.2006.09.007>.
- [31] J. Kratochvíl, D. Kahoun, J. Štěrba, H. Langhansová, J. Lieskovská, P. Fojtková, J. Hanuš, J. Kousal, O. Kylián, V. Straňák, Plasma polymerized C:H:N:O thin films for controlled release of antibiotic substances, *Plasma Process. Polym.* 15 (2018) 1700160, <https://doi.org/10.1002/ppap.201700160>.
- [32] J. Kratochvíl, D. Kahoun, O. Kylián, J. Štěrba, T. Kretková, J. Kousal, J. Hanuš, J. Václavová, V. Prýsiaznyh, P. Sezemský, P. Fojtková, J. Lieskovská, H. Langhansová, I. Krakovský, V. Straňák, Nitrogen enriched C:H:N:O thin films for improved antibiotics doping, *Appl. Surf. Sci.* 494 (2019) 301–308, <https://doi.org/10.1016/j.apsusc.2019.07.135>.
- [33] K. O'Donnell, A. Boyd, B.J. Meenan, Controlling fluid diffusion and release through mixed-molecular-weight poly(ethylene glycol) diacrylate (PEGDA) hydrogels, *Materials (Basel)* 12 (2019) 3381, <https://doi.org/10.3390/ma12203381>.
- [34] H.J. Busscher, H.C. van der Mei, G. Subbiahdoss, P.C. Jutte, J.J.A.M. van den Dungen, S.A.J. Zaai, M.J. Schultz, D.W. Grainger, Biomaterial-associated infection: locating the finish line in the race for the surface, *Sci. Transl. Med.* 4 (2012), <https://doi.org/10.1126/scitranslmed.3004528> 153rv10-153rv10.
- [35] K. Page, M. Wilson, I.P. Parkin, Antimicrobial surfaces and their potential in reducing the role of the inanimate environment in the incidence of hospital-acquired infections, *J. Mater. Chem.* 19 (2009) 3819, <https://doi.org/10.1039/b818698g>.
- [36] R. Kumar, H. Münstedt, Silver ion release from antimicrobial polyamide/silver composites, *Biomaterials* 26 (2005) 2081–2088, <https://doi.org/10.1016/j.biomaterials.2004.05.030>.
- [37] J. Harges, H. Ahrens, C. Gebert, A. Streitwieser, H. Buerger, M. Erren, A. Gunsel, C. Wedemeyer, G. Saxler, W. Winkelmann, Lack of toxicological side-effects in silver-coated megaprotheses in humans, *Biomaterials* 28 (2007) 2869–2875, <https://doi.org/10.1016/j.biomaterials.2007.02.033>.
- [38] L. Gao, L. Wang, L. Yang, Y. Zhao, N. Shi, C. An, Y. Sun, J. Xie, H. Wang, Y. Song, Y. Ren, Preparation, characterization and antibacterial activity of silver nanoparticle/graphene oxide/diatomite composite, *Appl. Surf. Sci.* 484 (2019) 628–636, <https://doi.org/10.1016/j.apsusc.2019.04.153>.
- [39] J. Günther, W. Petzl, I. Bauer, S. Ponsuksili, H. Zerbe, H.-J. Schuberth, R.M. Brunner, H.-M. Seyffert, Differentiating *Staphylococcus aureus* from *Escherichia coli* mastitis: *S. aureus* triggers unbalanced immune-dampening and host cell invasion immediately after udder infection, *Sci. Rep.* 7 (2017) 4811, <https://doi.org/10.1038/s41598-017-05107-4>.
- [40] S. Ferraris, M. Miola, A. Cochis, B. Azzimonti, L. Rimondini, E. Prenesti, E. Vernè, *In situ* reduction of antibacterial silver ions to metallic silver nanoparticles on bioactive glasses functionalized with polyphenols, *Appl. Surf. Sci.* 396 (2017) 461–470, <https://doi.org/10.1016/j.apsusc.2016.10.177>.
- [41] E. Greła, J. Kozłowska, A. Grabowiecka, Current methodology of MTT assay in bacteria — a review, *Acta Histochem.* 120 (2018) 303–311, <https://doi.org/10.1016/j.acthis.2018.03.007>.
- [42] Q.L. Feng, J. Wu, G.Q. Chen, F.Z. Cui, T.N. Kim, J.O. Kim, A mechanistic study of the antibacterial effect of silver ions on *Escherichia coli* and *Staphylococcus aureus*, *J. Biomed. Mater. Res.* 52 (2000) 662–668, [https://doi.org/10.1002/1097-4636\(20001215\)52:4<662::AID-JBMT10>3.0.CO;2-3](https://doi.org/10.1002/1097-4636(20001215)52:4<662::AID-JBMT10>3.0.CO;2-3).
- [43] A. Kędziora, M. Speruda, E. Krzyżewska, J. Rybka, A. Łukowiak, G. Bugla-Płoskońska, Similarities and differences between silver ions and silver in nanofoms as antibacterial agents, *Int. J. Mol. Sci.* 19 (2018) 444, <https://doi.org/10.3390/ijms19020444>.
- [44] J.R. Swathy, M.U. Sankar, A. Chaudhary, S. Aigal, Anshup, T. Pradeep, Antimicrobial silver: an unprecedented anion effect, *Sci. Rep.* 4 (2015) 7161, <https://doi.org/10.1038/srep07161>.
- [45] K. Vasilev, Nanoengineered antibacterial coatings and materials: a perspective, *Coatings* 9 (2019) 654, <https://doi.org/10.3390/coatings9100654>.
- [46] A. Abbaszadegan, Y. Ghahramani, A. Gholami, B. Hemmateenejad, S. Dorostkar, M. Nabavizadeh, H. Sharghi, The effect of charge at the surface of silver nanoparticles on antimicrobial activity against Gram-positive and Gram-negative bacteria: a preliminary study, *J. Nanomater.* 2015 (2015) 1–8, <https://doi.org/10.1155/2015/720654>.
- [47] J.S.R. Marins, L.M. Sassone, S.R. Fidel, D.A. Ribeiro, *In vitro* genotoxicity and cytotoxicity in murine fibroblasts exposed to EDTA, NaOCl, MTAD and citric acid, *Braz. Dent. J.* 23 (2012) 527–533, <https://doi.org/10.1590/S0103-64402012000500010>.
- [48] E.G. Zeferino, C.E.S. Bueno, L.M. Oyama, D.A. Ribeiro, *Ex vivo* assessment of genotoxicity and cytotoxicity in murine fibroblasts exposed to white MTA or white Portland cement with 15% bismuth oxide, *Int. Endod. J.* 43 (2010) 843–848, <https://doi.org/10.1111/j.1365-2591.2010.01747.x>.
- [49] M. Li, Y. Wang, Q. Liu, Q. Li, Y. Cheng, Y. Zheng, T. Xi, S. Wei, *In situ* synthesis and biocompatibility of nano hydroxyapatite on pristine and chitosan functionalized graphene oxide, *J. Mater. Chem. B* 1 (2013) 475–484, <https://doi.org/10.1039/C2TB00053A>.
- [50] C. Liao, Y. Li, S. Tjong, Bactericidal and cytotoxic properties of silver nanoparticles, *Int. J. Mol. Sci.* 20 (2019) 449, <https://doi.org/10.3390/ijms20020449>.
- [51] X. Yan, S. Li, Y. Pan, B. Xing, R. Li, B.W.-L. Jang, X. Liu, Tunable Ag<sup>+</sup> ion release from Ag@C for antibacterial and antifouling performances, *RSC Adv.* 5 (2015) 39384–39391, <https://doi.org/10.1039/C5RA02904J>.